

Predicting the Peak Energy of Swift Gamma-Ray Bursts Using Supervised Machine Learning

Wan-Peng Sun¹, Si-Yuan Zhu¹, Da-Ling Ma¹, and Fu-Wen Zhang^{1,2,*}

¹ College of Physics and Electronic Information Engineering, Guilin University of Technology, Guilin 541004, China

² Key Laboratory of Low-dimensional Structural Physics and Application, Education Department of Guangxi Zhuang Autonomous Region, Guilin 541004, China

ABSTRACT

Gamma-ray bursts (GRBs) are among the most energetic explosive phenomena in the universe, and their peak energy (E_p) is a key physical quantity for understanding the prompt emission mechanism. However, due to the limited energy coverage of the Swift satellite, a large fraction of Swift GRBs lack reliable measurements of the peak energy. Therefore, developing an accurate and efficient method to predict E_p is of great importance. In this work, we propose a method based on the SuperLearner framework that integrates multiple supervised machine learning algorithms to predict E_p of Swift/BAT GRBs. We use the Swift/BAT observational data from December 2004 to September 2022 as training features, and adopt the peak energies of 516 GRBs jointly detected by Swift and either Fermi/GBM or Konus-Wind as training labels. After training and testing multiple supervised models, the final SuperLearner ensemble yields a more robust and reliable predictive model. In 100 iterations of 5-fold cross validation, the predicted E_p' values show a tight correlation with the observed E_p , with an average Pearson correlation coefficient of $r = 0.72$. Compared with previous Bayesian estimates, our model provides predictions that are likely closer to the true values. Based on the trained model, we further predict the peak energies of 650 Swift GRBs, significantly increasing the number of GRBs with known peak energies and providing new statistical support for constraining GRB emission mechanisms and energy origins.

Key words. transients: gamma-ray bursts: general - methods: statistical: machine learning

1. Introduction

Gamma-ray bursts (GRBs) are among the most energetic and active high-energy transients in the Universe, serving as key probes of extreme physical processes. Their prompt emission directly traces the initial energy dissipation of ultra-relativistic jets, providing insight into jet dynamics and radiation mechanisms. This emission typically exhibits a non-thermal spectrum, which in the νF_ν representation shows a prominent peak, corresponding to the peak energy E_p . As a fundamental physical quantity characterizing the spectral properties, E_p reflects the characteristic energy of the radiating particles, encodes information on radiation mechanisms and jet dynamics (Lithwick & Sari 2001; Pe'er & Ryde 2011; Piran 2004), and plays a central role in spectrum-energy correlations. These include the $E_{p,z}$ - E_{iso} relation (known as the Amati relation), the $E_{p,z}$ - L_{iso} relation (Yonetoku relation), and other empirical correlations (Amati et al. 2002; Amati 2006; Wei & Gao 2003; Yonetoku et al. 2004; Ghirlanda et al. 2008; Liang et al. 2015), where $E_{p,z}$ is rest frame peak energy, $E_{p,z} = E_p \times (1 + z)$, E_{iso} and L_{iso} are the isotopic energy and peak luminosity of the GRB prompt emission, respectively. Such correlations establish GRBs as potential probes of high-redshift astrophysics and cosmology (Han et al. 2024, 2025; Du et al. 2025).

Accurately measuring E_p is challenging. Obtaining a reliable peak energy typically requires broadband spectral coverage—from tens of keV to several MeV—to capture the full spectral shape across both the low- and high-energy ranges. GRB spectra

are commonly fitted with a broken power-law function, typically represented by the Band function (Band et al. 1993), which consists of a low- and a high-energy components. In some cases, the spectra can also be well described by a cutoff power-law (CPL) model. For a subset of GRBs, the high-energy cutoff cannot be detected due to the limited energy range of the instruments, and their spectra are thus fitted with a simple power-law (PL) model (Sakamoto et al. 2008, 2011), making it difficult to determine the peak energy.

Thanks to its rapid and accurate localization capabilities, the Swift satellite has assembled a large sample of GRBs with measured redshifts, enabling deeper exploration of their intrinsic properties and progenitors, including the evolution of their early afterglows. However, the Swift/BAT detector operates in a relatively narrow energy range of 15-150 keV, which is significantly lower than the typical GRB prompt emission energies (tens of keV to several MeV) (Gruber et al. 2014; Bošnjak et al. 2014). As a result, Swift is often unable to provide reliable constraints on the spectral parameters during the prompt emission phase. Specifically, owing to the inherent limitations of the BAT detector, a large fraction of Swift GRBs have spectra that can be modeled only by a PL function (Zhang et al. 2007; Sakamoto et al. 2006). In such cases, the observed photon index Γ merely reflects the spectral slope along the tail of the Band function rather than the intrinsic low-energy index α , thereby obscuring the spectral curvature around the peak energy and preventing a reliable determination of their peak energies. Indeed, when Swift GRBs are jointly detected by other broad band instruments such as Konus-Wind or Fermi/GBM, their spectra can typically be fitted with

* Corresponding authors: fwzhang@pmo.ac.cn

the Band function; however, such joint detections account for only a small fraction of the Swift sample. Therefore, obtaining reliable estimates of E_p for Swift GRBs has long been a major challenge, which is crucial for systematically investigating the intrinsic radiation mechanisms of GRBs.

Several studies have attempted to estimate E_p using empirical correlations involving the spectral index (Virgili et al. 2012; Zhang et al. 2007; Sakamoto et al. 2006) or spectral hardness (Cui et al. 2005; Zhang et al. 2007; Shahmoradi & Nemiroff 2010). These works typically combine observations from multiple instruments to construct more reliable estimation models and results. However, linear relations constructed from only two parameters often exhibit large intrinsic scatter and strong sample dependence. In contrast, Butler et al. (2007) introduced a Bayesian approach that incorporates additional observational parameters and prior knowledge, yielding relatively more accurate estimates of E_p . More recently, Li & Wang (2024) exploited the spectral curvature within the BAT band to infer lower limits on E_p for bursts with $E_p > 150$ keV, providing a complementary pathway when direct constraints are unavailable.

However, traditional methods for estimating E_p are generally constrained by their reliance on crude, low-dimensional empirical correlations. To overcome this limitation, we seek methods capable of incorporating richer observational information and capturing the complex, nonlinear relationships between GRB observables and E_p . With the rapid advancement of data-driven techniques, machine learning (ML) provides precisely such capabilities and has been increasingly applied in astrophysics (Rodríguez et al. 2022; Fotopoulou 2024; Wang et al. 2025), including the classification of transient sources such as GRBs (Chen et al. 2024; Zhu et al. 2024, 2025a,b) and fast radio bursts (FRBs) (Luo et al. 2023; Sun et al. 2025, 2026), as well as the estimation of GRB redshifts (Aldowma & Razzaque 2024; Narendra et al. 2025). ML thus offers a flexible framework for modeling such high-dimensional dependencies. In this work, we focus on Swift GRB observations and apply supervised ML models to estimate E_p from multiple observable features.

The ML framework used in this study includes several base learners—Random Forest, Extreme Gradient Boosting, Linear Regression, and Kernel Ridge Regression—which, after extensive training, exhibit good stability and reliable generalization. These models are then integrated using the SuperLearner ensemble method, which assigns optimal weights based on cross-validated performance. This strategy has proven highly effective for predicting the redshifts of active galactic nuclei and GRBs (Dainotti et al. 2021; Narendra et al. 2022; Dainotti et al. 2024, 2025), enabling the ensemble to exploit the complementary strengths of individual algorithms and achieve enhanced predictive accuracy.

In Section 2, we describe the sample and the data selection criteria used in this work. In Section 3, we present the selection of predictive parameters, the dataset partitioning strategy, and a detailed discussion of the training and optimization of the supervised ML algorithms. Section 4 reports the main prediction results and compares the performance of the SuperLearner ensemble method with other approaches in estimating the peak energy of Swift GRBs. Finally, Section 5 summarizes our work.

2. Data Sample Selection

2.1. Data

Since 2004, Swift/BAT has continuously monitored the sky, providing a large dataset for GRB studies. In this work, we select BAT

observations from December 2004 to September 2022, retrieved from the Swift archive¹, comprising a total of 1557 GRBs (hereafter referred to as the BAT sample). Among them, 229 GRBs can be well fit with the CPL model and have reliably determined E_p values; these GRBs are therefore excluded from our generalization sample. The remaining 1328 GRBs can only be fitted with a PL model and lack measured E_p values.

For training the ML models, we use E_p values from GRBs simultaneously observed by Swift and the broad band instruments Fermi/GBM and Konus-Wind. The Fermi/GBM sample includes GRBs detected between June 2008 and September 2022 that are temporally coincident with Swift triggers and have consistent sky positions (RA/Dec), with data obtained from the online Fermi GRB catalog². The Konus-Wind sample consists of GRBs observed concurrently with Swift between December 2004 and September 2022, with data primarily drawn from Svinkin et al. (2016) and Tsvetkova et al. (2017, 2021). For both Fermi and Konus-Wind spectra, only GRBs whose spectra are best fitted by the Band or CPL functions are selected to ensure the reliability of E_p values.

2.2. Feature Selection and Dataset Partitioning

Based on previous experience, to ensure that supervised ML algorithms achieve stable and reliable generalization performance, it is necessary to use sufficiently large and balanced training samples. To satisfy these requirements while ensuring that basic observational parameters are available for each GRB, we select four physical parameters from the BAT sample as input features for training: spectral index (Γ , obtained from simple power-law fits), peak flux (F_p), fluence (S_γ), and duration (T_{90}) (hereafter, these four observational parameters are referred to as input features). GRBs lacking any of these four parameters are excluded, resulting in the removal of 162 GRBs. The final BAT sample thus contains 1166 GRBs with complete observational data, of which only 516 are simultaneously detected by Fermi or Konus-Wind and have reliable E_p measurements (248 observed by Fermi and 268 observed by Konus-Wind).

The sample is ultimately divided into a training set and a generalization set. The training set is used to train the ML models, enabling them to acquire stable and reliable generalization capability, while the generalization set is employed to estimate the originally unknown E_p values using the trained models. Specifically, the training set consists of 516 GRBs with reliable E_p measurements and corresponding BAT observational parameters, including 470 long GRBs (LGRBs) and 46 short GRBs (SGRBs), which are listed in Table 1. The generalization set comprises 650 GRBs lacking E_p values but possessing complete observational data, including 591 LGRBs and 59 SGRBs.

It is worth noting that ML models typically require the training data to exhibit approximately normal distributions. To better satisfy this condition, all three input features except Γ are used in logarithmic form. The parameter distributions for the training and generalization sets are displayed in Figure 1. From this figure, we find that the training set tends to have larger F_p and S_γ values and smaller Γ values compared to the generalization set, while the distributions of T_{90} appear broadly similar between the two sets. The distribution of E_p for the 516 GRBs in the training set is presented in Figure 2.

¹ <https://swift.gsfc.nasa.gov/archive/>

² <https://heasarc.gsfc.nasa.gov/W3Browse/fermi/fermigtrig.html>

Table 1: List of 516 BAT GRBs in the training set.

GRB	T_{90} (s)	F_p ($\text{ph cm}^{-2} \text{s}^{-1}$)	S_γ ($10^{-7} \text{ erg cm}^{-2}$)	Γ	E_p (keV)
GRB050126	24.80	0.71 ± 0.17	8.38 ± 0.80	1.34	158^{+82}_{-41}
GRB050315	95.60	1.93 ± 0.22	32.20 ± 1.46	2.11	47^{+4}_{-5}
GRB050318	32.00	3.16 ± 0.20	10.80 ± 0.77	1.90	34^{+8}_{-5}
GRB050401	33.30	10.70 ± 0.92	82.20 ± 3.06	1.40	105^{+14}_{-11}
GRB050505	58.90	1.85 ± 0.31	24.90 ± 1.79	1.41	99^{+20}_{-13}

Notes. Only a portion of this table is shown here for guidance. The full table is available in machine-readable format.

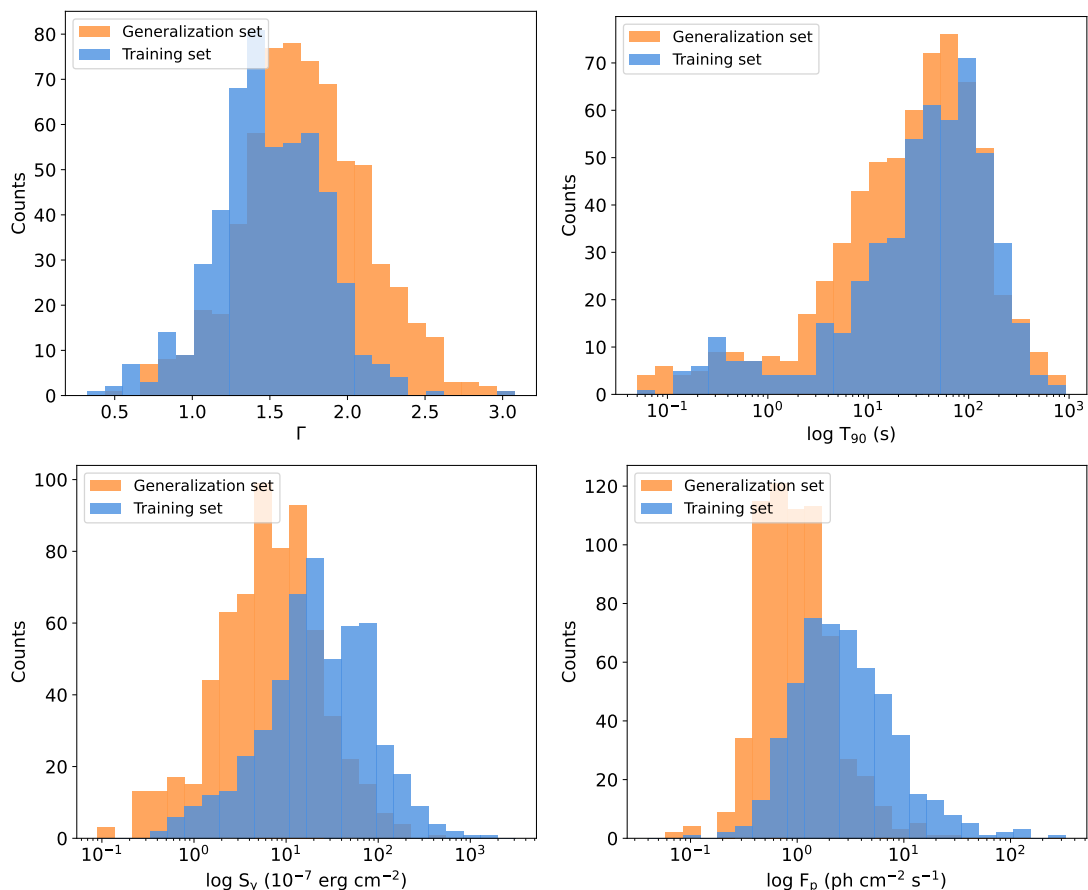


Fig. 1: Distributions of the four input quantities, Γ , T_{90} , S_γ , and F_p , for the training set (blue region) and the generalization set (orange region).

In addition, to better illustrate the relationships among the parameters in the training set, we present their correlation matrix in Figure 3. The results show that Γ exhibits the strongest negative correlation with E_p (Pearson's $r = -0.69$), followed by F_p ($r = 0.13$) and T_{90} ($r = -0.12$). Beyond linear correlation analysis, Figure 4 shows the relative feature importance derived from the random forest algorithm, which reflects the contribution of each input feature to the model's learning and prediction of E_p (see the next section for training details). The results indicate that Γ is the most informative feature, providing the dominant contribution to the prediction of E_p . In comparison, the other three parameters have weaker and relatively similar importances, with T_{90} ranking second among them.

3. Methodology

3.1. ML Algorithms

To obtain reliable estimates of E_p using supervised ML algorithms, we first train the models on the training set. To maximize model accuracy and ensure stable generalization, each algorithm is trained 100 times via random data resampling: in each iteration, 80% of the training set is used for model fitting, while the remaining 20% serves as a validation set (hereafter referred to as the test set). Model performance is evaluated by comparing the predicted E'_p with the known E_p in the test set, using the root-mean-square error (RMSE) and the Pearson correlation coefficient. This procedure is repeated 100 times, and the average results are used to assess model accuracy. Notably, each of the 100 random resampling iterations involves independent model

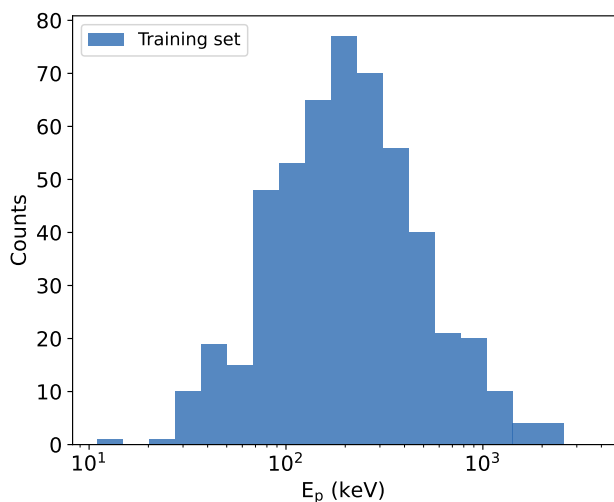


Fig. 2: The distribution of E_p in the training set.

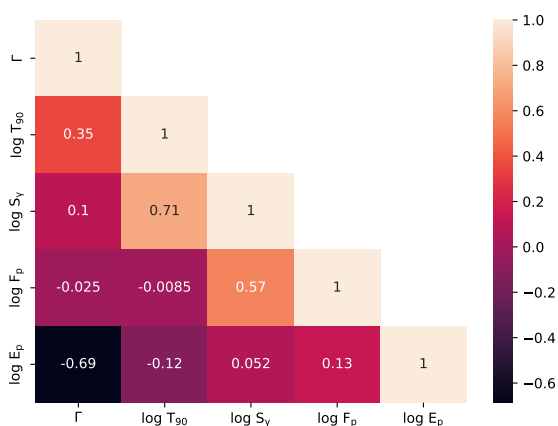


Fig. 3: Correlation heatmap of various parameters in the training set.

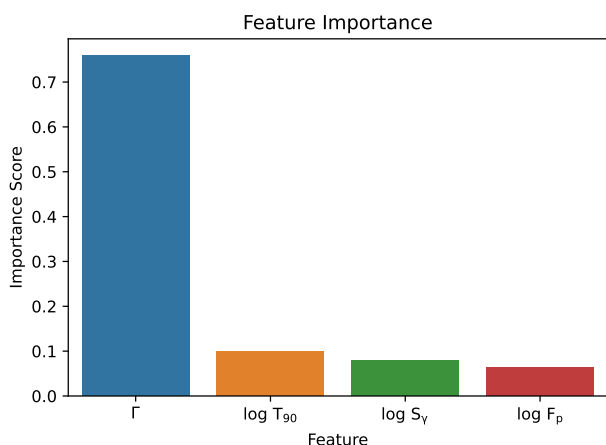


Fig. 4: Feature importance scores trained by the random forest algorithm, reflecting the relative importance of the four input features in the random forest training set.

training, ensuring that the evaluation is not affected by information leakage between different subsets and thus providing an unbiased assessment of model performance.

In the second step, the trained ML models are applied to predict E_p in the generalization set. We ultimately employ the SuperLearner technique to combine multiple trained models into a single ensemble, leveraging the strengths of each model to generate the predicted E_p' values. The individual predictions are then aggregated to produce the final estimates, allowing the SuperLearner to achieve greater accuracy than any single algorithm alone. The ML algorithms used in this work are listed below:

1. The Random Forest algorithm is an ensemble method based on decision trees. It constructs multiple independent decision trees, each trained separately, and combines their outputs to improve the accuracy of the final prediction (Breiman 2001). Random Forest has been widely applied in both classification and regression tasks, particularly excelling in handling high-dimensional and complex data. In addition, the algorithm is sensitive to outliers and requires careful consideration when evaluating feature importance and handling missing data. An important aspect of using Random Forest is selecting the optimal tree depth and the number of trees according to the complexity and structure of the data.
2. The Extreme Gradient Boosting (XGBoost) algorithm also achieves its performance by combining multiple decision trees and represents an improved version of gradient-boosted decision trees, addressing some limitations of traditional decision trees (Chen & Guestrin 2016). It enhances model accuracy by sequentially fitting the residuals of previous predictions, with each tree trained based on the errors of the preceding tree, thereby iteratively improving predictive performance. Additionally, XGBoost incorporates regularization to control tree complexity and prevent overfitting, and employs parallelization to accelerate computation, resulting in higher efficiency and prediction accuracy.
3. Linear Regression is one of the simplest and most widely used regression models. Its core idea is to establish a linear relationship between the predicted outcome and the input features, with model parameters estimated by minimizing the sum of squared errors.
4. Kernel Ridge Regression extends linear regression into the feature space. Unlike traditional ridge regression, the kernelized version replaces the inner product with a kernel function, allowing nonlinear patterns in the original low-dimensional space to be mapped into a higher-dimensional space. A ridge regression model is then constructed in this high-dimensional space to predict new data points. The algorithm also incorporates a regularization term to prevent overfitting, thereby improving the model's generalization ability.

3.2. Model Training and Optimization

During the training of supervised ML algorithms, hyperparameter tuning is performed to ensure that each algorithm achieves optimal performance on the data without underfitting or overfitting. Taking the Random Forest algorithm as an example, excessively deep trees can lead to overfitting and reduced generalization, whereas too few trees can result in underfitting and lower predictive accuracy. Therefore, methods such as cross validation and grid search are typically used to determine the optimal tree depth and number of trees. Generally, increasing the number of trees improves accuracy but also increases computational complexity, requiring a balance between predictive performance and efficiency.

In this work, the optimization criteria are the lowest RMSE and the highest Pearson correlation coefficient observed during tuning. The algorithms primarily optimized in this study are the tree-based ensemble methods, Random Forest and XGBoost. For Random Forest, the main hyperparameters adjusted include the number of trees and tree depth, while the maximum number of leaf nodes is kept at the default value due to the limited number of input features. The optimization process for Random Forest is illustrated in Figure 5, showing the algorithm’s performance across different tree numbers and depths. The lowest RMSE and highest Pearson correlation are achieved with a tree depth of 5 and 250 trees, which are adopted as the optimal hyperparameters in this study. All other parameters are set to their default values.

A similar optimization procedure is applied to the XGBoost algorithm. We first explore the dependence of model performance on the tree depth and the number of trees. As shown in Figures 6(a) and (b), the residuals and Pearson correlation coefficients indicate that the optimal configuration is achieved with a tree depth of 2 and 90 trees. We then fix the tree depth at this value and examine the impact of different learning rates for varying numbers of trees, as illustrated in Figures 6(c) and (d). These results show that the best performance is obtained with 90 trees and a learning rate of 0.07. All remaining XGBoost parameters are kept at their default settings. The linear regression model used in this work contains no essential tunable hyperparameters, while the kernel ridge regression model adopts a polynomial kernel with $\alpha = 0.6$, degree = 2, and coef0 = 2.5.

Different ML algorithms exhibit distinct strengths on the same dataset. In this work, we employ the SuperLearner algorithm to combine multiple models and maximize overall performance, with the detailed procedure described in the following subsection.

3.3. SuperLearner

After training each individual ML algorithm 100 times on randomly sampled datasets, we integrate them into a SuperLearner ensemble. SuperLearner is an ensemble method that combines multiple base algorithms using V-fold cross validation (van der Laan Mark J. et al. 2007). For a given dataset, it is often difficult to determine a priori which algorithm will perform best, and SuperLearner effectively addresses this challenge. During cross validation, it adaptively assigns higher weights to algorithms that are better suited to the current training data (hereafter also referred to as predictors) while reducing the weights of lower-performing models. Specifically, weights are assigned to each algorithm based on its residuals during cross validation, with algorithms producing lower residuals receiving higher coefficients; all coefficients are non-negative and sum to one. These properties allow SuperLearner to leverage the unique strengths of different algorithms, constructing an ensemble model that effectively minimizes prediction residuals.

In this work, we employ 5-fold cross validation, in which the training set of 516 GRBs is randomly divided into five complementary subsets. SuperLearner trains on four subsets while using the remaining subset as a validation set to guide model adjustment. This process is repeated five times so that each subset serves once as the validation set. During these iterations, SuperLearner automatically assigns optimal weights to each predictor based on the data, thereby optimizing the prediction of E_p across all validation sets. We repeat this entire procedure 100 times, i.e., performing 100 iterations of 5-fold cross validation with random data splits and model training, which allows for a robust assessment of the SuperLearner ensemble’s stability and reduces

dependence on any specific random data partition. Considering the limited size of the current BAT training sample and the accuracy of the observational data, this step is critical for evaluating and optimizing model performance.

Generally, using too many folds could make model training overly sensitive to local features within subsets, thereby reducing generalization, whereas too few folds limit the diversity of training samples, hindering effective learning. Therefore, we choose 5-fold cross validation to achieve a SuperLearner ensemble with stronger generalization, rather than 10- or 3-fold. In fact, our experiments confirm that this choice yields the best performance.

All ML algorithms in this work are implemented in Python. Random Forest, Linear Regression, and Kernel Ridge Regression are implemented using Scikit-learn³, XGBRegressor is from XGBoost⁴, and the SuperLearner ensemble is implemented using the Mlens package (v0.2.3)⁵.

4. Results and Analysis

4.1. Model Performance and Prediction Results

In this work, the final SuperLearner model used for both training and generalization integrates the four optimized predictors described in Section 3.1. Figure 7 presents the results from 100 independent random training runs, where the horizontal axis represents the observed E_p and the vertical axis shows the model-predicted E'_p . The red solid line denotes the best-fit relation, while the black solid lines indicate the 2σ uncertainty range. The results yield a Pearson correlation coefficient of $r = 0.725$ and a RMSE of 0.267 between the true and predicted E_p values. According to the outlier definition proposed by Jones & Singal (2020), only about 5% of the training data are identified as catastrophic outliers, i.e., GRBs with $|\Delta E_p| > 2\sigma$, which lie outside the black lines in Figure 7. Beyond training performance, the model’s behavior on the test set is of greater significance, as it provides a more realistic measure of predictive accuracy. Figure 8 illustrates a representative example of the SuperLearner’s performance on the test set, where the fraction of catastrophic outliers similarly remains at approximately 5%.

Figure 9 shows the distributions of the correlation coefficients and residuals obtained from 100 rounds of 5-fold cross validation. The results from these independent training runs demonstrate that, aside from a few special cases where the predictors exhibit slightly higher or lower performance, the overall generalization ability remains stable. The averaged performance across all runs yields a Pearson correlation coefficient of $r = 0.72$ and an RMSE of 0.27, providing a solid foundation for applying the trained model to the generalization sample.

Table 2 summarizes the performance comparison between the SuperLearner ensemble and the four individual predictors used in this study. Across 100 randomized training iterations, the SuperLearner consistently achieves higher average correlation coefficients and lower residuals, demonstrating its superior generalization performance.

4.2. Bias Correction

It can be seen from Figure 7 that some GRBs with low E_p are predicted with higher values, while those with high E_p are predicted with lower ones, a typical indication of prediction bias.

³ https://scikit-learn.org/stable/supervised_learning.html

⁴ <https://xgboost.ai/>

⁵ <http://ml-ensemble.com/>

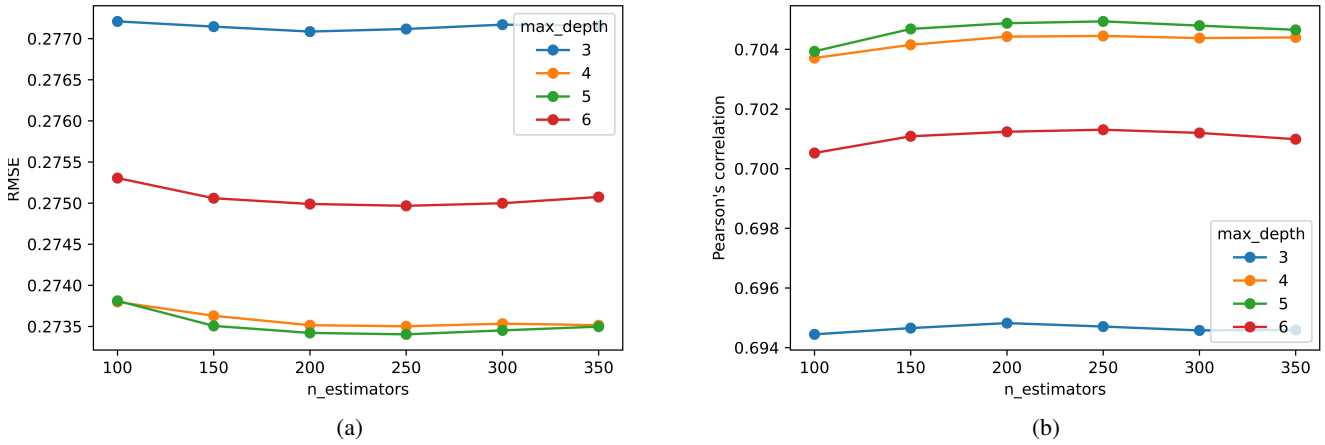


Fig. 5: Optimization plot of hyperparameters in the random forest algorithm. Panels (a) and (b) show the variations in RMSE and Pearson correlation coefficient with the number of trees and the maximum tree depth, respectively.

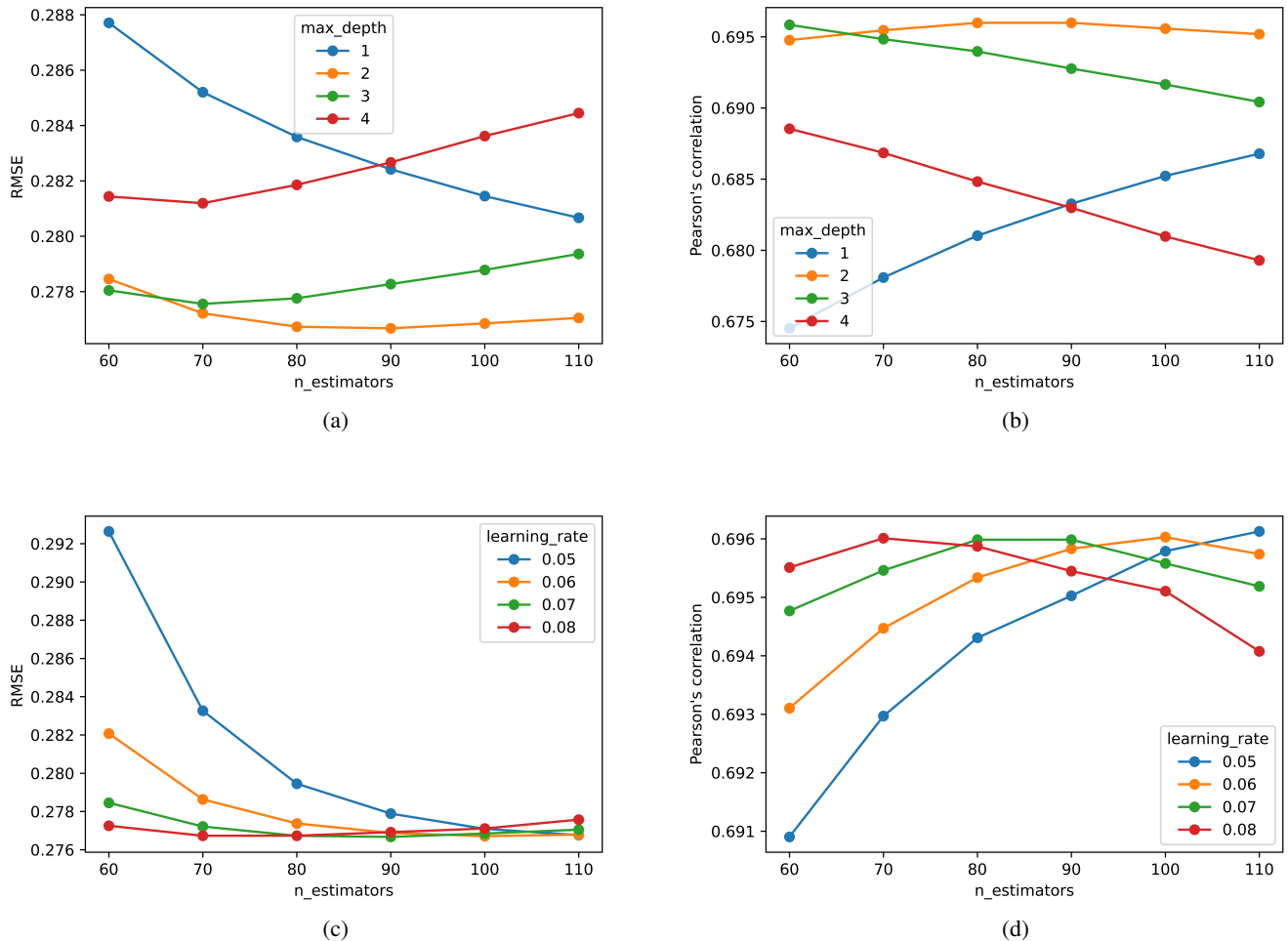


Fig. 6: Optimization of XGBoost hyperparameters. Panels (a) and (b) show the dependence of the RMSE and the Pearson correlation coefficient on the number of trees and the maximum tree depth, respectively. Panels (c) and (d) show their dependence on the number of trees and the learning rate, respectively.

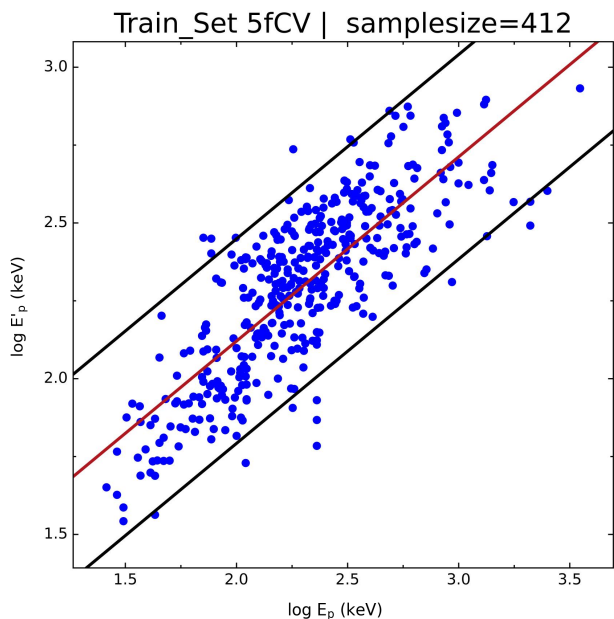


Fig. 7: Relation between the predicted peak energy (E'_p) obtained with the SuperLearner model and the observed peak energy (E_p) for the training set. The red solid line shows the best-fit relation, while the black solid lines mark the 2σ confidence bounds.

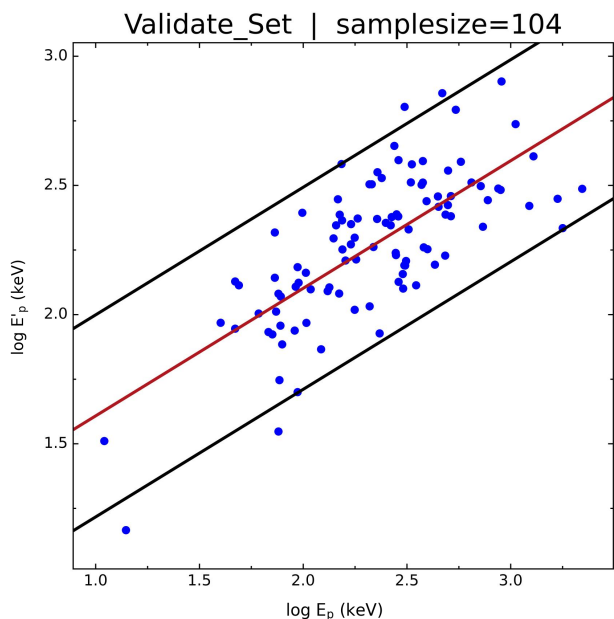


Fig. 8: Relation between the predicted peak energy (E'_p) obtained with the SuperLearner model and the observed peak energy (E_p) for the test set. The red solid line denotes the best-fit relation, and the black solid lines indicate the corresponding 2σ confidence bounds.

Such bias usually arises from data imbalance; e.g., low- or high- E_p GRBs are relatively scarce in the observed sample, preventing the model from being adequately trained on these regions. How-

Table 2: Performance comparison between the SuperLearner and the four individual predictors.

Algorithm	r	RMSE
SuperLearner	0.72	0.267
Random Forest Regressor	0.70	0.274
XGBoost Regressor	0.70	0.277
Kernel Ridge	0.71	0.269
Linear Regression	0.70	0.273

ever, data imbalance is not the only cause. Limitations in the intrinsic performance of the learning algorithm or the presence of more complex nonlinear relations between input features and E_p at the low or high ends may also contribute to this issue.

We fit a linear relation between the predicted E'_p and the observed E_p to correct for systematic bias. The correction formula is expressed as

$$\log E'_p = a \times \log E_p + b, \quad (1)$$

where E'_p and E_p denote the predicted and observed peak energies, respectively, and a and b are the slope and intercept of the linear fit. In this work, we obtain $a = 0.606$ and $b = 0.902$. This makes it possible to correct the bias in the predictions of the generalization set, which is discussed in the following subsection.

4.3. Prediction on the Generalization Set

In this section, we apply the model to estimate the peak energies of 650 GRBs in the generalization set. The final prediction results are presented in Table 3. Figure 10 compares the distributions of E'_p in the generalization set and E_p in the training set. A substantial overlap is observed between the two distributions. However, the predicted E'_p values in the generalization set are systematically lower. As discussed in Section 2.2, the four predictive variables in the generalization set exhibit distinct distributional differences from those in the training sample. Specifically, F_p and S_γ are generally lower, while Γ tends to be higher. Considering the positive correlations of E_p with S_γ and F_p and its inverse correlation with Γ (as shown in the correlation heatmap in Figure 3), the overall lower E'_p values predicted for the generalization set are therefore physically reasonable.

We further examine the overall distribution of peak energies in the BAT sample by considering both the training and generalization sets as a single dataset. Observations from the past decade by the Fermi satellite provide a useful reference (von Kienlin et al. 2020; Poolakkil et al. 2021), as the GBM's wide energy coverage and large sample size make it highly representative. Figure 11 compares E_p distributions of the BAT and GBM samples, showing that the BAT sample generally exhibits lower E_p values.

To more specifically characterize the differences of peak energy, we show the following statistical results: the BAT sample exhibits an E_p range of 4-3516 keV with a median value of 152 keV, whereas the GBM sample spans 24-5092 keV with a median value of 214 keV. Obviously, while the BAT GRBs cover a broader E_p range, their average peak energy is lower than that of the GBM GRBs. This discrepancy likely arises from the intrinsically broader energy coverage of GBM, whereas BAT's sensitivity at lower energies may bias the measurements of predictive parameters (e.g., lower F_p and S_γ), which in turn affects the estimated E_p . Beyond instrumental effects, limitations in the ML models also contribute to residual biases. To further mitigate

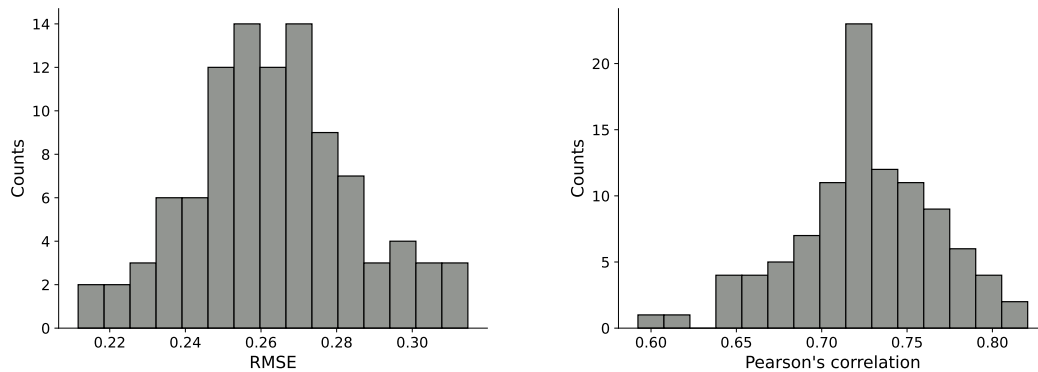


Fig. 9: The left and right panels show the distributions of root mean squared error and Pearson correlation coefficient, respectively, over 100 runs of 5-fold cross validation.

Table 3: List of 650 BAT GRBs in the generalization set.

GRB	T_{90} (s)	F_p ($\text{ph cm}^{-2} \text{s}^{-1}$)	S_γ ($10^{-7} \text{ erg cm}^{-2}$)	Γ	E'_p (keV)	Bias-corrected E'_p (keV)
GRB041219C	4.80	2.45 ± 0.25	13.10 ± 0.73	2.02	57	26
GRB041220	5.60	1.81 ± 0.14	3.83 ± 0.28	1.66	114	80
GRB041223	109.10	7.35 ± 0.32	167.00 ± 2.79	1.11	465	820
GRB041226	89.70	0.35 ± 0.05	3.21 ± 0.83	1.40	392	619
GRB041228	55.40	1.61 ± 0.25	34.90 ± 1.52	1.60	168	152

Notes. Only a portion of this table is shown here for guidance. The full table is available in machine-readable format. The ‘Bias-corrected E'_p ’ refers to E'_p after applying bias corrections.

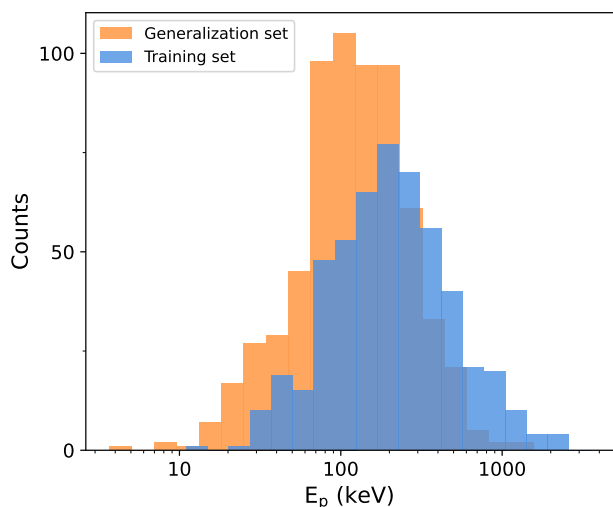


Fig. 10: Comparison of the peak energy distribution of 516 GRBs in the training set (blue region) with that of 650 GRBs in the SuperLearner generalization set (orange region).

potential biases in the predicted E'_p , we apply the correction formula described in Section 4.2; the corrected results are listed in Table 3. After correction, the highest predicted E'_p in the generalization set exceeds 6000 keV, and the number of GRBs with $E'_p > 200$ keV increases substantially, better reflecting the true distribution of GRB peak energies. The present results are based on training with only 516 GRBs, and the dataset size remains limited. Nevertheless, the proposed model provides a valuable

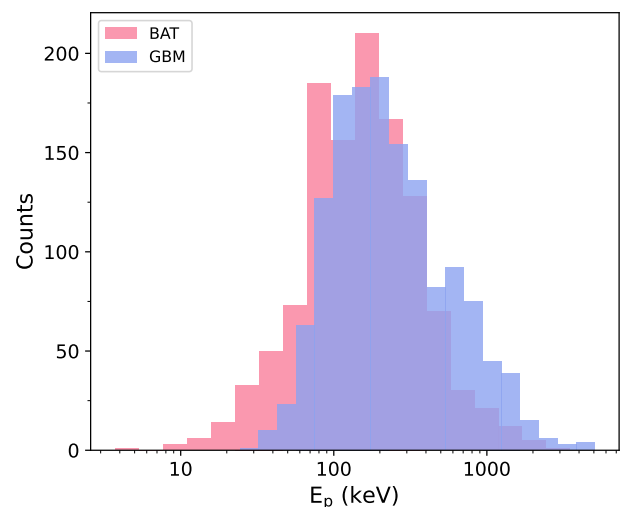


Fig. 11: Distribution of peak energy of GRBs in the BAT and GBM samples. The purple region represents the BAT sample, which is composed of the training set and the generalization set in this work. The green region represents the GBM sample, which is composed of observational data from Fermi between 2008 and 2018.

framework for estimating the peak energies of BAT GRBs. As future joint observations from Fermi, Konus-Wind, and Swift accumulate more GRB data, this limitation is expected to be alleviated, enabling more reliable predictions of BAT GRB peak energies.

4.4. Spectrum-Energy Correlations

The Amati and Yonetoku relations are two of the most widely studied spectrum-energy correlations in GRBs (Amati et al. 2002; Yonetoku et al. 2004; Amati 2006; Zhang et al. 2012; Ito et al. 2019). By estimating peak energies for a large Swift sample, we examine these correlations in the BAT GRBs. We compile the most comprehensive redshift dataset currently available for BAT GRBs, including 392 GRBs with complete redshift and parameter measurements (Table 4). The redshift information is primarily taken from the website⁶. This large sample provides a valuable opportunity to revisit the spectrum-energy correlations of GRBs.

To derive the isotropic peak energies (E_{iso}) and luminosities (L_{iso}) for these 392 GRBs, we consider both the Band and CPL models. Specifically, for BAT GRBs for which the CPL model is identified as the best fit and for which the low-energy spectral index α and other observational parameters are available, we use the CPL model in the calculations. For the majority of GRBs that are only fitted with PL model, we adopt the Band model to estimate, assigning typical values of $\alpha = -1$ and $\beta = -2.25$ for the low- and high-energy spectral indices, respectively (Preece et al. 2000).

The isotropic energy and luminosity of a GRB are derived from the following relations, with all values corrected to the 1 – 10000 keV energy band:

$$E_{\text{iso}} = \frac{4\pi D_L^2 S_\gamma k}{(1+z)}, \quad (2)$$

$$L_{\text{iso}} = 4\pi D_L^2 F_p k, \quad (3)$$

where D_L is the luminosity distance, S_γ and F_p denote the time-integrated fluence and peak flux, respectively, and k is the correction factor, defined as

$$k = \frac{\int_{1/(1+z)}^{10^4/(1+z)} EN(E)dE}{\int_{e_{\text{min}}}^{e_{\text{max}}} EN(E)dE}, \quad (4)$$

with e_{min} and e_{max} representing the instrument's energy band, and $N(E)$ denoting the GRB spectral model. In this work, we adopt the Band and CPL spectral forms as in Equations 5 and 6:

$$N(E) = \begin{cases} A \left(\frac{E}{100 \text{ keV}}\right)^\alpha \exp\left(-\frac{E}{E_0}\right), & E < (\alpha - \beta)E_0, \\ A \left(\frac{E}{100 \text{ keV}}\right)^\beta \left[\frac{(\alpha - \beta)E_0}{100 \text{ keV}}\right]^{\alpha - \beta} \\ \quad \times \exp(\beta - \alpha), & E \geq (\alpha - \beta)E_0, \end{cases} \quad (5)$$

$$N(E) = A \left(\frac{E}{100 \text{ keV}}\right)^\alpha \exp\left(-\frac{E}{E_c}\right), \quad (6)$$

where α and β are the low- and high-energy photon spectral indices, and E_c and E_0 denote the cutoff energies, with $E_c = E_0 = E_p/(2 + \alpha)$, where E_p is the peak energy. The final calculated values are listed in Table 4, with all uncertainties propagated via standard error propagation.

⁶ <https://www.mpe.mpg.de/~jcg/grbgen.html>

Figures 12 and 13 show the Amati and Yonetoku relations for LGRBs, respectively. Orange and green circles denote GRBs with measured E_p (285 GRBs) and those with predicted E'_p from the SuperLearner model (81 GRBs). We analyze all LGRBs together, with the red solid line representing the best-fit relation. Using a least-squares fitting, we obtain the Amati relation for the Swift/BAT LGRB sample as

$$\log E_{p,z} = (-14.67 \pm 1.05) + (0.33 \pm 0.02) \times \log E_{\text{iso}}. \quad (7)$$

This result is consistent with previous studies (Minaev & Pozanenko 2020; Zhu et al. 2023). In our BAT sample, a clear positive correlation persists between $\log E_{p,z}$ and $\log E_{\text{iso}}$ for LGRBs, with a Pearson correlation coefficient of $r = 0.65$ and a slope of $a = 0.33$. We find that the 366 LGRBs in our BAT sample are consistent with the updated Amati relation reported recently by Li (2023).

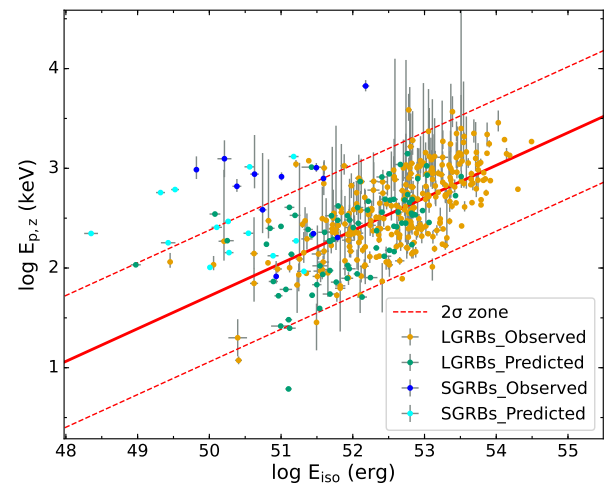


Fig. 12: Relationship between $E_{p,z}$ and E_{iso} of BAT GRBs. Deep blue (light blue) dots represent SGRBs in the training (generalization) set, and orange (green) dots represent LGRBs in the training (generalization) set. The solid red line represents the best-fit line for all LGRBs, and the dashed line represents the 2σ confidence interval.

Similarly, analysis of the LGRB sample reveals a very tight correlation between $\log E_{p,z}$ and $\log L_{\text{iso}}$, as shown in Figure 13. Both the predicted and observed LGRBs follow a consistent trend, with no noticeable differences. Furthermore, we fit the correlation between the peak energy and the isotropic luminosity for LGRBs, yielding the following Yonetoku relation:

$$\log E_{p,z} = (-9.53 \pm 0.59) + (0.24 \pm 0.01) \times \log L_{\text{iso}}. \quad (8)$$

The Pearson correlation coefficient between $E_{p,z}$ and L_{iso} is 0.73, with a slope of $a = 0.24$. This slope is somewhat lower than that reported in most previous studies (Zhang et al. 2012, 2018; Zhu et al. 2023), although some works have also found coefficients around 0.2 (Xu et al. 2023). It remains uncertain whether this deviation originates from the prediction errors in E'_p , from intrinsic variations in a larger sample, or from selection effects. Nevertheless, the existence of a Yonetoku relation in our LGRB sample is well supported.

Table 4: Properties of BAT GRBs with Redshift.

GRB	T_{90} (s)	F_p (ph cm ⁻² s ⁻¹)	S_γ (10 ⁻⁷ erg cm ⁻²)	α	β	z	$E_{p,z}$ (keV)	log E_{iso} (erg)	log L_{iso} (erg s ⁻¹)
GRB050126	24.80	0.71 ± 0.17	8.38 ± 0.80	-1	-2.25	1.29	362 ⁺¹⁸⁸ ₋₉₄	51.84 ^{+0.04} _{-0.04}	51.04 ^{+0.10} _{-0.10}
GRB050315	95.60	1.93 ± 0.22	32.20 ± 1.46	-1	-2.25	1.949	139 ⁺¹² ₋₁₅	52.82 ^{+0.02} _{-0.02}	50.28 ^{+0.05} _{-0.05}
GRB050318	32.00	3.16 ± 0.20	10.80 ± 0.77	-1	-2.25	1.44	83 ⁺²⁰ ₋₁₂	52.12 ^{+0.03} _{-0.03}	50.18 ^{+0.03} _{-0.03}
GRB050401	33.30	10.70 ± 0.92	82.20 ± 3.06	-1	-2.25	2.9	410 ⁺⁵⁵ ₋₄₃	53.56 ^{+0.02} _{-0.02}	51.47 ^{+0.04} _{-0.04}
GRB050505	58.90	1.85 ± 0.31	24.90 ± 1.79	-1	-2.25	4.27	522 ⁺¹⁰⁵ ₋₆₉	53.29 ^{+0.03} _{-0.03}	51.09 ^{+0.07} _{-0.07}
GRB210420B*	158.80	0.50 ± 0.20	15.00 ± 2.00	-1	-2.25	1.4	467	52.22 ^{+0.06} _{-0.06}	51.04 ^{+0.17} _{-0.17}
GRB210504A*	135.06	0.90 ± 0.20	27.00 ± 2.00	-1	-2.25	2.077	545	52.76 ^{+0.03} _{-0.03}	51.69 ^{+0.10} _{-0.10}
GRB210517A*	3.06	1.50 ± 0.20	1.50 ± 0.30	-1	-2.25	2.486	334	51.70 ^{+0.09} _{-0.09}	50.45 ^{+0.06} _{-0.06}
GRB211023B*	1.30	2.20 ± 0.30	1.70 ± 0.30	-1	-2.25	0.862	133	50.89 ^{+0.08} _{-0.08}	49.47 ^{+0.06} _{-0.06}
GRB211024B*	603.50	0.90 ± 0.20	68.00 ± 3.00	-1	-2.25	1.1137	481	52.72 ^{+0.02} _{-0.02}	51.10 ^{+0.10} _{-0.10}

Notes. Only a portion of this table is shown here for guidance. The full table is available in machine-readable format. An asterisk (*) denotes GRBs in the generalization set. The columns α and β represent the low-energy and high-energy photon indices, respectively. For BAT GRBs that can only be fitted with a PL model, we adopt $\alpha = -1$ and $\beta = -2.25$ of the Band function to calculate the values of E_{iso} and L_{iso} . If the best-fit spectral model is CPL, only the low-energy photon index is listed.

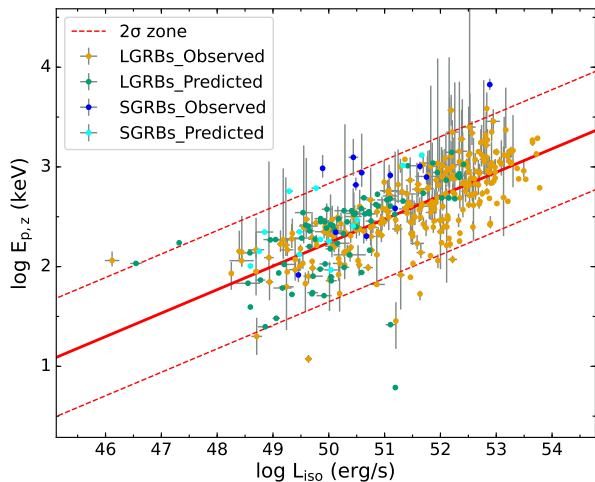


Fig. 13: Relationship between $E_{p,z}$ and L_{iso} of BAT GRBs. The caption is the same as that of Figure 12.

In addition, the SGRBs with measured E_p and those with predicted E'_p are shown as dark and light blue circles in Figures 12 and 13, respectively. Since only 26 SGRBs have known redshifts, the limited number of data points is insufficient to reliably constrain the spectrum-energy correlations for SGRBs. Therefore, we do not plot the fitting correlation lines for them. Nevertheless, we attempt to fit the spectrum-energy relations of SGRBs, and the corresponding results are summarized in Table 5.

Interestingly, the fitting parameters of the Yonetoku relation are found to be very similar between LGRBs and SGRBs, indicating that their $E_{p,z}$ - L_{iso} correlations are largely consistent. This similarity suggests that LGRBs and SGRBs may share similar radiation mechanisms, as also reported in several previous studies (Zhang et al. 2009; Ghirlanda et al. 2009; Guiriec et al. 2013; Zhu et al. 2023). Overall, our results provide a large Swift sample of 392 GRBs for spectrum-energy correlation analysis, showing that the 366 LGRBs in the Swift catalog still follow the Amati and Yonetoku correlations.

5. Discussion

Since the Bayesian method to estimate GRB peak energies was proposed by Butler et al. (2007), it has been widely adopted. We collect 728 predicted peak energies of GRBs from the on-line repository of Butler et al. (2007) up to December 2018. To evaluate the performance of the SuperLearner method, we select 419 GRBs for which the predicted peak energies are available from both methods (i.e., the overlapping sample) for comparison. As shown in Figure 14, the peak energies of GRBs predicted by the Bayesian method tend to be lower than those estimated by the SuperLearner. After accounting for the 90% credible intervals of the Bayesian estimates, the predicted peak energies from the two methods are broadly consistent for the majority of GRBs. However, for approximately 18% (77/419) of the GRBs, the SuperLearner predictions fall outside the Bayesian credible intervals. These discrepancies largely arise because the Bayesian upper bounds are often too low to encompass the higher E'_p values inferred by the SuperLearner.

To more directly assess the discrepancy between predicted and observed values, we further select 309 GRBs from 2004–2018 with both reliable observed E_p and Bayesian-derived $E'_{p,B}$ (Figure 15). The horizontal axis represents the observed E_p , and the vertical axis shows the Bayesian-predicted $E'_{p,B}$. It is evident that the Bayesian estimates are systematically lower than the observed values, particularly for $E_p > 60$ keV. Furthermore, even when simultaneously accounting for the Bayesian 90% credible intervals and the reported observational uncertainties of the observed E_p , $\sim 14\%$ (44/309) of the GRBs show no overlap between the two ranges. Importantly, in these non-overlapping cases, the observed peak energies predominantly exceed the Bayesian upper bounds. Both the comparison with the SuperLearner predictions and the direct observational validation consistently indicate a systematic underestimation of peak energies by the Bayesian approach. Taken together, these comparisons provide indirect evidence that the SuperLearner predictions are likely less biased and closer to the intrinsic peak energies.

To further assess the reliability of the SuperLearner model, we compile the CPL-fitted peak energies ($E_{p,\text{CPL}}$) of 229 GRBs from the BAT sample, which obtained from <https://swift.gsfc.nasa.gov/results/>

Table 5: The results of regression analysis for spectrum-energy correlations, in which r is the correlation coefficient, p is the chance probability, and σ is the dispersion.

	Correlations	Expressions	r	p	σ
LGRB	$E_{p,z}(E_{\text{iso}})$	$\log E_{p,z} = (-14.67 \pm 1.05) + (0.33 \pm 0.02) \times \log E_{\text{iso}}$	0.65	$< 10^{-4}$	0.33
	$E_{p,z}(L_{\text{iso}})$	$\log E_{p,z} = (-9.53 \pm 0.59) + (0.24 \pm 0.01) \times \log L_{\text{iso}}$	0.73	$< 10^{-4}$	0.30
SGRB	$E_{p,z}(E_{\text{iso}})$	$\log E_{p,z} = (-3.05 \pm 5.26) + (0.11 \pm 0.10) \times \log E_{\text{iso}}$	0.21	0.29	0.45
	$E_{p,z}(L_{\text{iso}})$	$\log E_{p,z} = (-14.15 \pm 2.94) + (0.33 \pm 0.06) \times \log L_{\text{iso}}$	0.75	$< 10^{-4}$	0.30

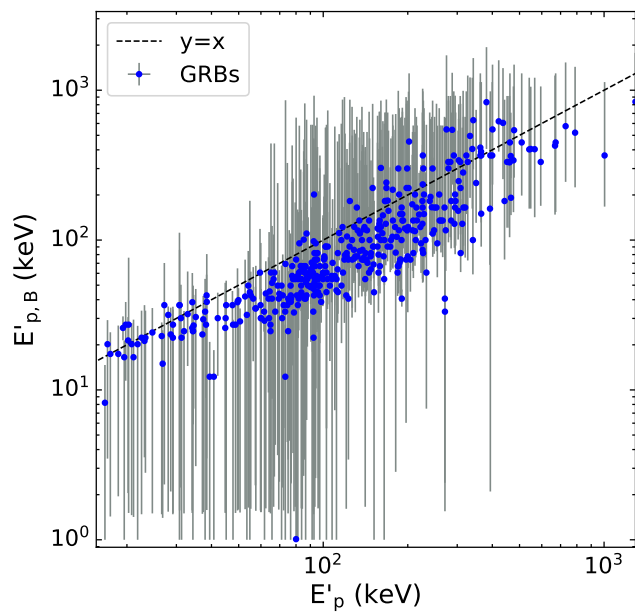
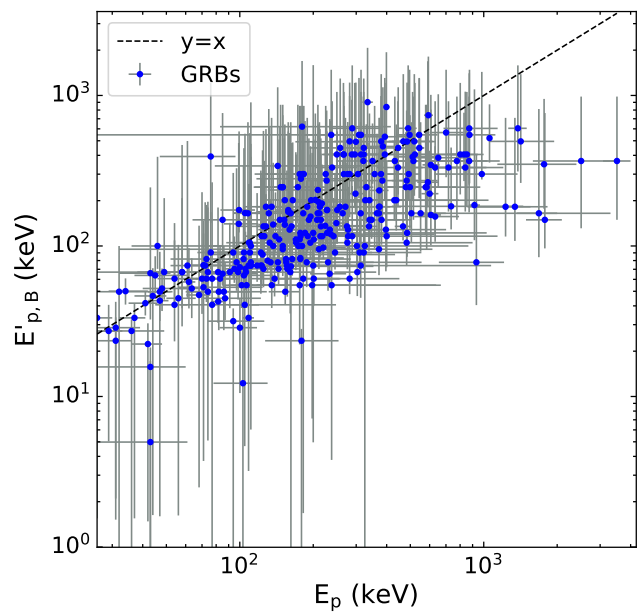

Fig. 14: Comparison of the predicted peak energy from the SuperLearner (E'_p) and the Bayesian ($E'_{p,B}$) methods.


Fig. 15: Comparison of the observed peak energy with the predicted peak energy derived from the Bayesian method.

batgrbcat/index_tables.html. The predicted peak energies of these GRBs are then estimated with the SuperLearner ensemble and compared with the $E_{p,\text{CPL}}$. Figure 16 shows the relation between the SuperLearner-predicted E'_p and $E_{p,\text{CPL}}$. It is evident that $E_{p,\text{CPL}}$ tends to be systematically lower than E'_p . This discrepancy arises because Swift/BAT is primarily sensitive to low energies, which limits its ability to constrain the prompt radiation spectrum. As a result, direct spectral fitting of Swift GRBs tends to systematically underestimate the peak energy (Cabrera et al. 2007). In contrast, the SuperLearner model trained with the peak energies measured by Fermi/GBM or Konus-Wind effectively alleviates this bias, thereby indirectly confirming the physical reliability of its predictions.

6. Conclusions

In this study, we propose a SuperLearner-based framework that integrates multiple supervised ML algorithms to predict the peak energy of Swift GRBs using multidimensional observational parameters, including Γ , F_p , S_γ , and T_{90} . This method fully exploits the intrinsic correlations among these quantities, overcoming the limitations of traditional statistical methods in modeling nonlinear relationships, thereby enabling a more accurate and robust estimation of GRB peak energies. The main conclusions of this study are summarized as follows:

1. Through 100 iterations of 5-fold cross validation, the SuperLearner model achieves an average RMSE of 0.27 and a correlation coefficient of $r = 0.72$ on the test set, demonstrating superior generalization performance compared to individual algorithms.
2. Furthermore, a comparison with the Bayesian estimation method proposed by Butler et al. (2007) shows that the SuperLearner predictions are more consistent with the true peak energies. This work therefore provides a new and more reliable approach for predicting the peak energies of Swift GRBs.
3. Based on this method, we predict the peak energies for 650 GRBs in the BAT sample. To account for potential biases introduced by ML algorithms, we further perform bias correction on the predicted values, and the corrected results are listed in Table 3.
4. Using the predicted peak energies together with 392 GRBs with measured redshifts, we revisit the $E_{p,z}-E_{\text{iso}}$ and $E_{p,z}-L_{\text{iso}}$ correlations for the Swift sample. The results show that both the Amati and Yonetoku relations remain evident for 366 LGRBs in the BAT sample. Although the number of SGRBs in this analysis is limited, their distribution in the Yonetoku relation exhibits a nearly identical trend to that of LGRBs, suggesting that the two classes may share similar radiation mechanisms.

This study represents the first attempt to predict GRB peak energies by combining multidimensional observational param-

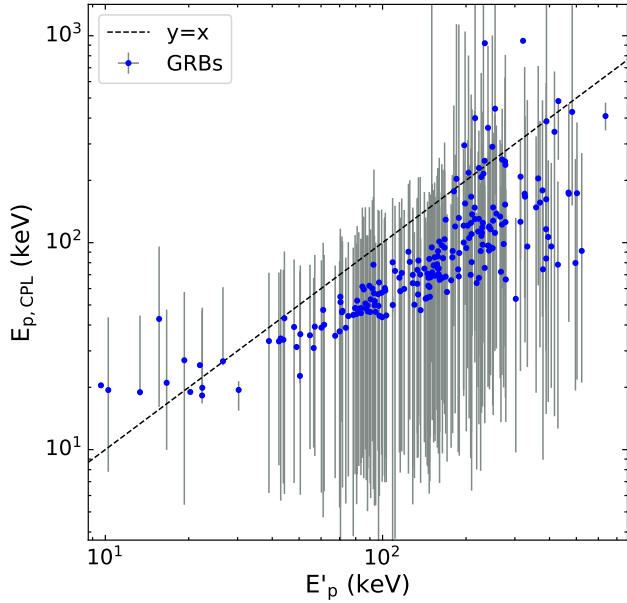


Fig. 16: Comparison between the peak energies estimated from the SuperLearner method and those obtained from the CPL model fitting.

eters with supervised ML techniques. The proposed approach benefits from both the extensive observational data accumulated by multiple detectors and the rapid advancement of ML methodologies, offering a new perspective and tool for GRB peak energy estimation. As more observational data become available, we will further optimize the model to improve prediction accuracy and provide more robust data support for GRB studies.

Acknowledgements. This work was supported in part by the National Natural Science Foundation of China (No. 12463008), and by the Guangxi Natural Science Foundation (No. 2022GXNSFDA035083).

References

- Aldowma, T. & Razzaque, S. 2024, *MNRAS*, 529, 2676
 Amati, L. 2006, *Monthly Notices of the Royal Astronomical Society*, 372, 233
 Amati, L., Frontera, F., Tavani, M., et al. 2002, *A&A*, 390, 81
 Band, D., Matteson, J., Ford, L., et al. 1993, *ApJ*, 413, 281
 Bošnjak, Ž., Götz, D., Bouchet, L., Schanne, S., & Cordier, B. 2014, *A&A*, 561, A25
 Breiman, L. 2001, *Mach. Learn.*, 45, 5–32
 Butler, N. R., Kocevski, D., Bloom, J. S., & Curtis, J. L. 2007, *ApJ*, 671, 656
 Cabrera, J. I., Firmani, C., Avila-Reese, V., et al. 2007, *MNRAS*, 382, 342
 Chen, J.-M., Zhu, K.-R., Peng, Z.-Y., & Zhang, L. 2024, *MNRAS*, 527, 4272
 Chen, T. & Guestrin, C. 2016, in *Proceedings of the 22nd ACM SIGKDD International Conference on Knowledge Discovery and Data Mining, KDD '16* (New York, NY, USA: Association for Computing Machinery), 785–794
 Cui, X.-H., Liang, E.-W., & Lu, R.-J. 2005, *Chinese J. Astron. Astrophys.*, 5, 151
 Dainotti, M. G., Bhardwaj, S., Cook, C., et al. 2025, *ApJS*, 277, 31
 Dainotti, M. G., Bogdan, M., Narendra, A., et al. 2021, *ApJ*, 920, 118
 Dainotti, M. G., Taira, E., Wang, E., et al. 2024, *ApJS*, 271, 22
 Du, G.-H., Li, T.-N., Ling, J.-L., et al. 2025 [arXiv:2510.26355]
 Fotopoulou, S. 2024, *Astronomy and Computing*, 48, 100851
 Ghirlanda, G., Nava, L., Ghisellini, G., Celotti, A., & Firmani, C. 2009, *A&A*, 496, 585
 Ghirlanda, G., Nava, L., Ghisellini, G., Firmani, C., & Cabrera, J. I. 2008, *Mon. Not. Roy. Astron. Soc.*, 387, 319
 Gruber, D., Goldstein, A., Weller von Ahlefeld, V., et al. 2014, *ApJS*, 211, 12
 Guiriec, S., Daigne, F., Hascoët, R., et al. 2013, *ApJ*, 770, 32
 Han, T., Jin, S.-J., Zhang, J.-F., & Zhang, X. 2024, *Eur. Phys. J. C*, 84, 663

- Han, T., Zhang, J.-F., & Zhang, X. 2025 [arXiv:2504.17741]
 Ito, H., Matsumoto, J., Nagataki, S., et al. 2019, *Nature Communications*, 10, 1504
 Jones, E. & Singal, J. 2020, *PASP*, 132, 024501
 Li, L. 2023, *ApJS*, 266, 31
 Li, L. & Wang, Y. 2024, arXiv e-prints, arXiv:2412.08226
 Liang, E.-W., Lin, T.-T., Lü, J., et al. 2015, *ApJ*, 813, 116
 Lithwick, Y. & Sari, R. 2001, *ApJ*, 555, 540
 Luo, J.-W., Zhu-Ge, J.-M., & Zhang, B. 2023, *MNRAS*, 518, 1629
 Minaev, P. Y. & Pozanenko, A. S. 2020, *MNRAS*, 492, 1919
 Narendra, A., Dainotti, M. G., Sarkar, M., et al. 2025, *A&A*, 698, A92
 Narendra, A., Gibson, S. J., Dainotti, M. G., et al. 2022, *ApJS*, 259, 55
 Pe'er, A. & Ryde, F. 2011, *ApJ*, 732, 49
 Piran, T. 2004, *Reviews of Modern Physics*, 76, 1143
 Poolakkil, S., Preece, R., Fletcher, C., et al. 2021, *ApJ*, 913, 60
 Preece, R. D., Briggs, M. S., Mallozzi, R. S., et al. 2000, *ApJS*, 126, 19
 Rodriguez, J.-V., Rodriguez-Rodriguez, I., & Woo, W. L. 2022, *WILEY INTERDISCIPLINARY REVIEWS-DATA MINING AND KNOWLEDGE DISCOVERY*, 12
 Sakamoto, T., Barthelmy, S. D., Barbier, L., et al. 2008, *ApJS*, 175, 179
 Sakamoto, T., Barthelmy, S. D., Baumgartner, W. H., et al. 2011, *ApJS*, 195, 2
 Sakamoto, T., Sato, G., Barbier, L., et al. 2006, in *AAS/High Energy Astrophysics Division*, Vol. 9, AAS/High Energy Astrophysics Division #9, 17.04
 Shahmoradi, A. & Nemiroff, R. J. 2010, *MNRAS*, 407, 2075
 Sun, W.-P., Zhang, J.-G., Li, Y., et al. 2025, *ApJ*, 980, 185
 Sun, W.-P., Zhang, Y.-K., Zhang, J.-G., et al. 2026, *ApJ*, 998, 339
 Svinkin, D. S., Frederiks, D. D., Aptekar, R. L., et al. 2016, *ApJS*, 224, 10
 Tsvetkova, A., Frederiks, D., Golenetskii, S., et al. 2017, *ApJ*, 850, 161
 Tsvetkova, A., Frederiks, D., Svinkin, D., et al. 2021, *ApJ*, 908, 83
 van der Laan Mark J., C. P. E., & E., H. A. 2007, *Statistical Applications in Genetics and Molecular Biology*, 6, 1
 Virgili, F. J., Qin, Y., Zhang, B., & Liang, E. 2012, *MNRAS*, 424, 2821
 von Kienlin, A., Meegan, C. A., Paciesas, W. S., et al. 2020, *ApJ*, 893, 46
 Wang, Z.-N., Qiang, D.-C., & Yang, S. 2025, *Universe*, 11, 355
 Wei, D. M. & Gao, W. H. 2003, *MNRAS*, 345, 743
 Xu, F., Huang, Y.-F., Geng, J.-J., et al. 2023, *A&A*, 673, A20
 Yonetoku, D., Murakami, T., Nakamura, T., et al. 2004, *ApJ*, 609, 935
 Zhang, B., Zhang, B.-B., Liang, E.-W., et al. 2007, *ApJ*, 655, L25
 Zhang, B., Zhang, B.-B., Virgili, F. J., et al. 2009, *ApJ*, 703, 1696
 Zhang, B. et al. 2007, *Astrophys. J.*, 655, 989
 Zhang, F.-W., Shao, L., Yan, J.-Z., & Wei, D.-M. 2012, *ApJ*, 750, 88
 Zhang, Z. B., Zhang, C. T., Zhao, Y. X., et al. 2018, *PASP*, 130, 054202
 Zhu, S.-Y., Deng, H.-Y., Zhang, F.-W., Mo, Q.-Z., & Tam, P.-H. T. 2025a, *MNRAS*, 541, 3236
 Zhu, S.-Y., Liu, Z.-Y., Shi, Y.-R., et al. 2023, *ApJ*, 950, 30
 Zhu, S.-Y., Shao, L., Tam, P.-H. T., & Zhang, F.-W. 2025b, *A&A*, 702, A173
 Zhu, S.-Y., Sun, W.-P., Ma, D.-L., & Zhang, F.-W. 2024, *MNRAS*, 532, 1434